

## Key Points:

- Gamma-Ray Spectrometer data reveal Mercury's northern hemisphere's average hydrogen abundance to be  $300_{-150}^{+250}$  ppm
- We produced the first neutron-derived hydrogen map, which shows an increase at the north pole of 75 ppm over equatorial values
- At midlatitudes a hydrogen-surface temperature anticorrelation is seen, with less hydrogen at Mercury's hot poles than at its cold poles

## Supporting Information:

- Supporting Information S1
- Data Set S1

## Correspondence to:

J. T. Wilson,  
jack.wilson@jhuapl.edu

## Citation:

Wilson, J. T., Lawrence, D. J., Peplowski, P. N., & Feldman, W. C. (2019). MESSENGER gamma ray spectrometer and epithermal neutron hydrogen data reveal compositional differences between Mercury's hot and cold poles. *Journal of Geophysical Research: Planets*, 124, 721–733. <https://doi.org/10.1029/2018JE005871>

Received 31 OCT 2018

Accepted 25 JAN 2019

Accepted article online 19 FEB 2019

Published online 7 MAR 2019

## Author Contributions:

**Conceptualization:** Jack T. Wilson, David J. Lawrence, Patrick N. Peplowski

**Formal analysis:** Jack T. Wilson, Patrick N. Peplowski

**Funding acquisition:** David J. Lawrence, Patrick N. Peplowski  
(continued)

©2019. The Authors.

This is an open access article under the terms of the Creative Commons Attribution-NonCommercial-NoDerivs License, which permits use and distribution in any medium, provided the original work is properly cited, the use is non-commercial and no modifications or adaptations are made.

# MESSENGER Gamma Ray Spectrometer and Epithermal Neutron Hydrogen Data Reveal Compositional Differences Between Mercury's Hot and Cold Poles

Jack T. Wilson<sup>1</sup> , David J. Lawrence<sup>1</sup> , Patrick N. Peplowski<sup>1</sup> , and William C. Feldman<sup>2</sup>

<sup>1</sup>The Johns Hopkins University Applied Physics Laboratory, Laurel, MD, USA, <sup>2</sup>Planetary Science Institute, Tucson, AZ, USA

**Abstract** The presence of hydrogen, most likely in the form of water ice, is well established in Mercury's permanently shaded polar craters. But lower concentrations that may exist away from the poles have not previously been well constrained. In this work we use data from the MErcury Surface, Space ENvironment, GEOchemistry, and Ranging (MESSENGER) Gamma-Ray and Neutron Spectrometer to produce the first map of the absolute hydrogen abundance in Mercury's northern hemisphere. We find a mean abundance of  $300_{-150}^{+250}$  ppm and a latitudinal trend that agrees with earlier results showing enhanced hydrogen contained within Mercury's radar bright craters. Additionally, we observe a middle- and low-latitude variation in hydrogen abundance that is correlated most strongly with temperature 20 cm beneath Mercury's surface.

**Plain Language Summary** Hydrogen, in water, is known to be present in Mercury's cold, dark polar craters. However, the distribution and abundance of hydrogen away from the poles remains unknown. Using data from the MErcury Surface, Space ENvironment, GEOchemistry, and Ranging (MESSENGER) Gamma-Ray and Neutron Spectrometer we present the first map of hydrogen in Mercury's northern hemisphere.

## 1. Introduction

Since the early 1990s, it has been believed that water ice is present in the permanently shadowed craters at Mercury's poles. An increase in same-sense radar backscatter was seen from an Earth-based radar within a few degrees of Mercury's poles at 3.5- (Butler et al., 1993; Slade et al., 1992), 12.6- (Harmon & Slade, 1992), and 70-cm (Black et al., 2010) wavelengths. Later high-resolution radar observations revealed this increased backscatter to be coincident with craters identified in Mariner 10 observations (Harcke, 2005; Harmon et al., 1994, 2001). As Mercury's obliquity is only  $2.029 \pm 0.085$  arc min (Stark et al., 2015) some craters at its poles are located in permanent shadow. With no atmosphere to conduct heat and a poorly conducting surface, the permanently shaded regions (PSRs) near the poles are expected to remain cold enough to retain water ice over geologically long timescales (Paige et al., 1992; Vasavada et al., 1999).

The data returned by MErcury Surface, Space ENvironment, GEOchemistry, and Ranging (MESSENGER) spacecraft (Solomon et al., 2007) have strengthened the association between the PSRs and water ice. Data from the Mercury Dual Imaging System (MDIS) and the Mercury Laser Altimeter (MLA) provided spectral reflectance and topography maps of Mercury's north polar region. The spectral reflectance data from MLA and MDIS have revealed dark and bright features consistent with the presence of both buried and surficial water ice and other volatiles (Chabot et al., 2014; Neumann et al., 2013). Topography maps from MLA data were used to derive temperature maps of the locations in and around the north polar PSRs (Paige et al., 2013). At the north pole, neutron measurements from MESSENGER's Gamma-Ray and Neutron Spectrometer (GRNS; Goldsten et al., 2007) revealed the presence of hydrogen-rich material that is consistent with the presence of 50–100 wt% water ice within Mercury's north polar PSRs (Lawrence et al., 2013). We note that these neutron data only reported hydrogen variations as a latitudinal profile in the northern hemisphere.

Lawrence et al. (2013) made use of intermediate-energy epithermal neutrons, which provide a sensitive measure of the bulk H abundances of near-surface planetary materials. Epithermal neutrons are defined as those with energy between 0.5 eV and 0.5 MeV. They are produced by nuclear spallation reactions when galactic

**Methodology:** Jack T. Wilson, David J. Lawrence, Patrick N. Peplowski, William C. Feldman

**Project administration:** David J. Lawrence

**Supervision:** David J. Lawrence

**Validation:** Jack T. Wilson

**Visualization:** Jack T. Wilson

**Writing - original draft:** Jack T. Wilson

**Writing - review & editing:** Jack T. Wilson, David J. Lawrence, Patrick N. Peplowski, William C. Feldman

cosmic rays (GCRs) collide with particles in planetary atmospheres or the surfaces of airless or nearly airless planetary bodies. Hydrogen atoms have a strong effect on the flux of epithermal neutrons due to their ability to moderate neutrons, a consequence of the similarity in mass between the neutron and hydrogen nucleus. Moderate amounts of hydrogen variability (i.e., a few hundred parts per million hydrogen) can cause detectable variations in epithermal neutrons. On the MESSENGER spacecraft, epithermal neutrons were measured with the Neutron Spectrometer (NS) portion of the GRNS (Goldsten et al., 2007).

In addition to neutron measurements, gamma ray measurements can provide information about hydrogen abundances via the 2,223-keV gamma ray line associated with the inelastic collision of neutrons with H nuclei (Boynton et al., 2002). However, this is only viable for footprint-averaged abundances greater than about 0.5 wt%, which are not seen on Mercury since the north polar PSRs are significantly smaller than the nominal GRNS spatial footprint in that region (Lawrence et al., 2011). An alternative route was proposed by Evans and Squyres (1987) and first demonstrated in Peplowski, David, et al. (2015). In this approach the ratio of gamma ray lines produced from inelastic collision and neutron-capture processes from a single element is combined with knowledge of the total macroscopic neutron absorption cross section ( $\Sigma_a$ ) to estimate the hydrogen abundance.

On the Moon, nonpolar hydrogen has been observed by the Lunar Prospector's Neutron Spectrometer (Lawrence, Patrick, et al., 2015). Correlation between the neutron-derived map and several measures of maturity (e.g., optical maturity; Lucey et al., 2000), Christiansen Feature position, and 750-nm albedo led to the conclusion that hydrogen abundance was also a measure of lunar regolith maturity. This is understood as the result of older regolith being subject to more solar wind proton implantation than do younger ones. On Mercury, maturity has been measured using crater density (Fassett et al., 2011) and Mercury Maturity Index (MMI; Neish et al., 2013), but the relationship of these parameters with bulk hydrogen concentration has not yet been examined.

Here we present a map of the variation of the epithermal neutron flux from Mercury. Using the method of estimating hydrogen abundance from gamma ray line ratios, we determine an absolute mean value for Mercury's northern hemisphere. This absolute value, in combination with the results of particle transport models, is then used to convert the epithermal neutron map into a hydrogen abundance map in Mercury's northern hemisphere. In section 2 we give a brief overview of the MESSENGER GRNS data acquisition, including a description of the data used in this study along with the data reduction that has been performed. In section 3 we present the result of the analysis. In section 4, we compare the map to other available data sets, including temperature, crater density, and MMI, and we provide a discussion and conclusion in section 5.

## 2. Data and Methods

In this study we use all the available MESSENGER GRNS data from 12 August 2004 until 30 April 2015. These data are available from the Planetary Data System at [http://pds-geosciences.wustl.edu/missions/messenger/ns\\_edr.html](http://pds-geosciences.wustl.edu/missions/messenger/ns_edr.html) and [http://pds-geosciences.wustl.edu/missions/messenger/grs\\_edr.html](http://pds-geosciences.wustl.edu/missions/messenger/grs_edr.html). Details of the GRNS are described by Goldsten et al. (2007). The epithermal neutron flux was obtained from the borated plastic (BP) single-event interactions spectra following the description in Lawrence et al. (2013). For each set of gain-corrected spectra a power law was fit to the nonpeak section to estimate the background. This power law fit was then subtracted from the spectra, and the total remaining counts within a channel window were summed to obtain the epithermal neutron counts.

As in previous studies of the MESSENGER neutron data (Lawrence et al., 2013, 2017; Peplowski, Bazell, et al., 2015), we will carry out the data reduction on both the measured data and a high-fidelity model time series. In the model, the planet's surface is taken to be compositionally uniform. Therefore, we would expect the map from the reduced model time series to be uniform if the data reduction process is successful. We will use this as a check in section 3 (see supporting information to Lawrence et al., 2013, for details of the modeling).

### 2.1. MESSENGER Epithermal Neutron Data Set Cuts

To avoid spurious results, data acquired during solar energetic particle (SEP) events were removed before the data were used. Following earlier studies (Lawrence et al., 2013, 2017), the duration of these events was determined manually by looking through the spectra for increased background (see the list of SEP events given in Lawrence et al., 2016). Similarly, those data acquired during energetic electron events (EEEs;

Lawrence, Anderson, et al., 2015; Nikoukar et al., 2018) were also removed as they complicate the derivation of neutron count rates. This removal of EEEs resulted in the loss of just a few spectra per orbit.

Additionally, cuts were required where the signal-to-noise ratio (SNR) of the data was particularly low due to the presence of the spacecraft between the planet and the detector. This led to the removal of data outside of the range  $-45^\circ < \text{nadir angle} < 90^\circ$  or  $87^\circ < x\text{-axis angle} < 93^\circ$ , where the nadir angle is that angle between the spacecraft  $z$ -axis and the vector connecting the spacecraft center to Mercury's center and, similarly, the  $x$ -axis angle is the angle between the spacecraft  $x$ -axis and spacecraft to planet vector. The spacecraft  $x$ -axis is the solar panel rotation axis, the  $y$ -axis is parallel to the magnetometer boom, and the  $z$ -axis completes the set to form a right-handed (for details, see Figure 1 in Lawrence et al., 2010). Also, the data taken when the spacecraft was greater than 1,500 km from the planet were removed due to the poor SNR caused by the signal's falling off with the square of the distance from the surface. Finally, the data are constrained to the northern hemisphere due to the low SNR in the south.

## 2.2. MESSENGER Epithermal Neutron Data Reduction

The data reduction procedures used to derive the epithermal neutron map are similar to those used for previous analyses of MESSENGER neutron data (Lawrence et al., 2010, 2013, 2017; Peplowski, Bazell, et al., 2015). As with earlier NS data sets including those from Lunar Prospector, Mars Odyssey, and Dawn, the MESSENGER data need to be corrected for several factors including variation in GCR flux, solid angle subtended by the target, and the detector's look direction. Additionally, due to MESSENGER's highly eccentric orbit, there are other corrections to be made. First, variations in altitude introduce large systematic effects that must be removed from the data set. Second, the thermal environment at Mercury and other operational constraints requires that the sunshade maintain a near-constant orientation relative to the Sun, which causes large variations in the look direction of the NS that need to be corrected. Finally, the spacecraft velocity changes during the course of an orbit inducing systematic count rate variations in the detected neutron signal. These variations are known as a Doppler effect (Feldman & Drake, 1986) and result from the fact that the speed of thermal and epithermal neutrons is similar to that of the spacecraft in orbit about Mercury (few kilometers per second). Because of these similar speeds, the neutron count rates systematically vary depending on the look direction of the detector. The neutron Doppler effect has been characterized for neutron measurements in prior missions with circular orbits where the directionality of the effect is tangential to the planetary surface (e.g., Maurice et al., 2004, 2011). However, the MESSENGER orbit around Mercury induces a radial Doppler effect that is perpendicular to the tangential variation. Corrections for this radial Doppler effect have not yet been attempted for orbital neutron measurements. In addition, as the dynamic variation in the neutron count rate is considerably lower on Mercury due to the small compositional variation across the planet's surface, these corrections must be performed with significant accuracy to recover statistically robust compositional information.

Following Lawrence et al. (2013, 2017), we implemented a parallel data-reduction pipeline operating on both the measured data and a modeled time series. The model was based on Monte Carlo N-Particle eXtended (MCNPX) neutron transport simulations of the emission and detection of neutrons from Mercury's surface and the detector. The particles' transport was calculated based on the analytical methods described in Feldman et al. (1989). Further details of this framework are provided in prior studies (Lawrence et al., 2010, 2013, 2017; Peplowski, Bazell, et al., 2015).

The reduction of the epithermal neutron data presented here is similar to that described in Lawrence et al. (2013) with several notable additions: (1) We utilize the data from the full 4 years of Mercury orbital data, whereas Lawrence et al. (2013) only used the first 10 months. This larger amount of data reduces the statistical uncertainties and allows for the creation of a northern hemisphere map of epithermal neutrons. (2) By making use of the Gamma-Ray Spectrometer (GRS)-derived hydrogen data, we will convert this epithermal neutron map into an absolute hydrogen abundance map, rather than report the results as changes in hydrogen abundance. (3) As these data cover a wider range in time, the GCR flux varies considerably during the duration of the measurements, which leads to larger systematic variations in epithermal neutron production than those in Lawrence et al. (2013). The measurement of GCR variability at Mercury used here is taken from Lawrence et al. (2016), and the empirical correction for the changing GCR flux is described below. (4) Following Peplowski, Bazell, et al. (2015), we implemented a two-dimensional correction for angle- and altitude-dependent NS-viewing response.

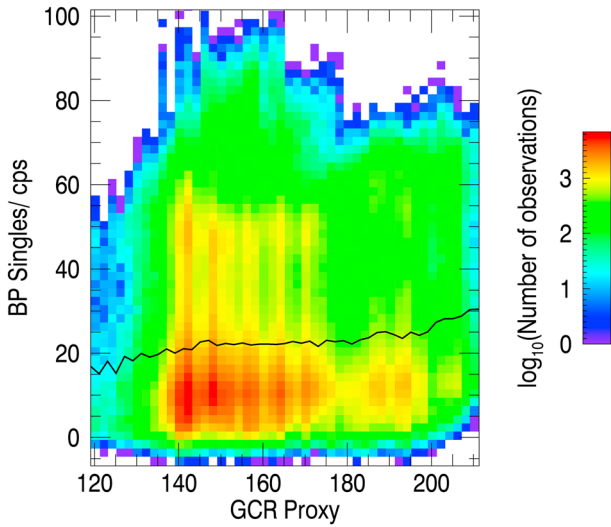


**Figure 1.** Density plot showing the variation of epithermal neutron counts per second against the galactic cosmic ray (GCR) proxy. The black line shows the mean borated plastic (BP) value in each GCR bin.

### 2.2.1. GCR Correction

The corrections in the following subsections were applied to both the data and the model. However, as the effective GCR flux does not vary in the model, this correction is carried out only on the measured epithermal neutron data. As Mercury-originating neutrons are the product of the interaction of GCRs with surface nuclei, their fluxes are directly proportional to the GCR flux at the planet's surface. The GCR flux is measured via the NS triple coincidence mode where protons with energies greater than 120 MeV are detected as they trigger all three NS sensors in coincidence. This triple coincidence count rate is a reliable proxy for the GCR flux variation (Lawrence et al., 2016).

The empirical GCR correction is illustrated in Figure 1, which shows the change in measured epithermal neutron counts with GCR proxy before any corrections are applied to the data. To derive the correction, the mean epithermal BP single measurement in a GCR proxy bin was calculated (black line in Figure 1). The BP data were then normalized by this value by interpolating to the relevant GCR proxy for each BP measurement and dividing the neutron measurement by the interpolated average for the given GCR proxy.

### 2.2.2. Nadir- and Solid-Angle Correction

The solid angle of the planet subtended at the spacecraft has a clear effect on the detected count rate due to the inverse square-like drop-off in neutron flux. A related trend is seen in the relationship between mean count rates and nadir angle, due to the pointing of the detector. As both of these effects result in changing the angular size of the planet seen from the detector, it is necessary to correct them simultaneously. This need is apparent in Figure 2, which shows how the change in count rate with changing solid angle varies with nadir angle. If these corrections were independent, one would expect the curve shown to have a constant value. The figure and related correction use only data taken when the spacecraft was south of 45°N to avoid contamination with the polar hydrogen signal. The solid-angle correction for the simulated and measured data was carried out as follows. First, the data were separated into a set of nadir-angle bins. Then in each of these bins an empirical linear relationship between count rate and solid angle was determined. That is, the parameters  $a$  and  $b$  were determined in the relation

$$f_{SA}(\theta_{NA}, \Omega) = a(\theta_{NA})\Omega + b(\theta_{NA}), \quad (1)$$

where  $\theta_{NA}$  is the nadir angle and  $\Omega$  the solid angle subtended by the planet at the spacecraft's position. The functional form of  $a$  is shown in Figure 2, and a similar function has been derived for  $b$ . Finally, for each measurement in the time series, an interpolated solid-angle slope and offset were determined from the measured solid angle and the values of Figure 2. The data were then corrected using the following algorithm:

$$C_1 = C_0 - f_{SA}(\theta_{NA}, \Omega) + f_{SA}(\theta_{NA,reference}, \Omega_{400}), \quad (2)$$

where  $C_0$  and  $C_1$  are the initial and corrected counts, respectively.

### 2.2.3. Doppler Correction

Two separate empirical Doppler corrections are applied to each of the model and data. The first is a multiplicative correction, of the form

$$c_{Doppler} = \frac{|\mathbf{v}_v| + \mathbf{v}_{sc} \cdot \hat{\mathbf{r}}}{|\mathbf{v}_v|}, \quad (3)$$

where  $\mathbf{v}_{sc}$  is the spacecraft velocity,  $\hat{\mathbf{r}}$  is the normal vector in the radial direction (i.e., the direction away from the center of Mercury), and  $|\mathbf{v}_v|$  takes the place of the neutron velocity. As  $|\mathbf{v}_v|$  is not measured, it is

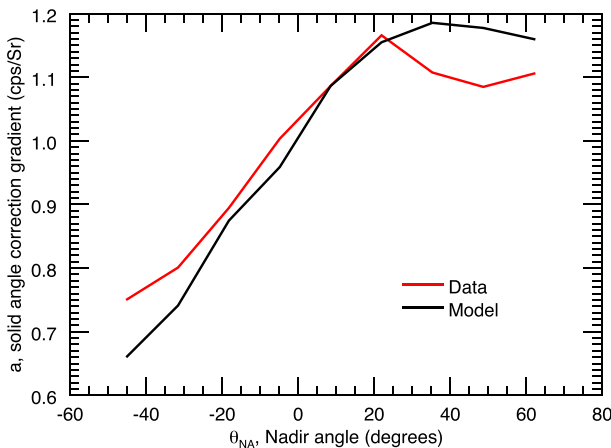


**Figure 2.** The slope of the solid-angle correction for each nadir angle. The actual slope used in the correction is interpolated from the calculated values.

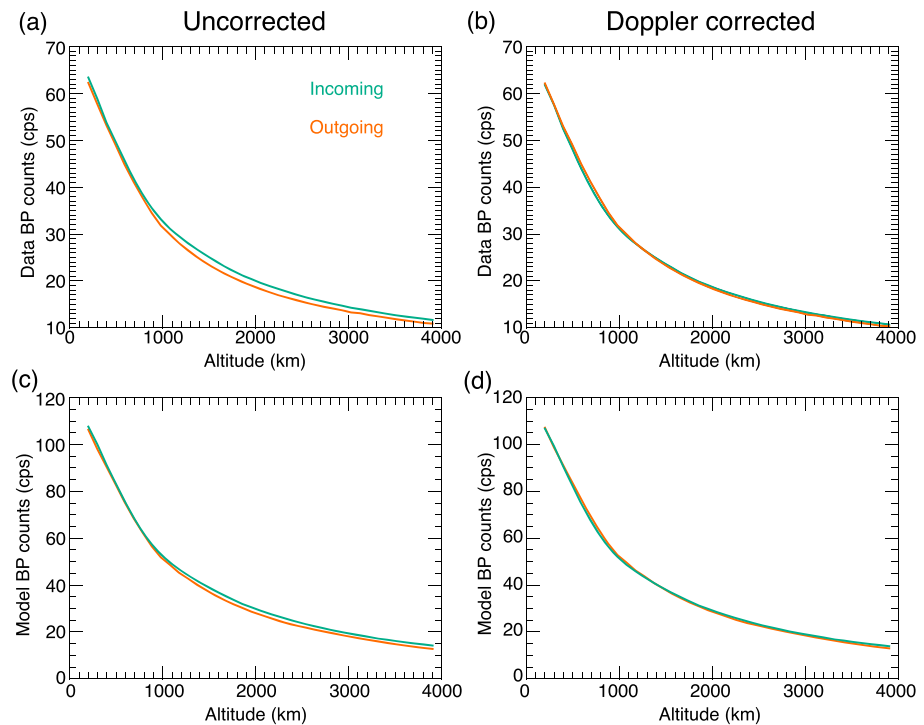


**Figure 3.** Mean borated plastic (BP) single epithermal neutron count rate versus spacecraft altitude for incoming (i.e., observations with a positive  $z$ -component of the velocity) and outgoing (i.e., observations with a negative  $z$ -component of velocity) spacecraft velocities, both in the measured data (a) before the Doppler correction and (b) after correction and in the model (c) before and (d) after the Doppler correction described by equation (3). The uncorrected plots illustrate the differences in count rate between measurements taken with positive and negative radial velocities due to Doppler shift. After correction, the lines from these two different classes of measurement overlap, showing the correction to be successful.

chosen empirically to minimize the misfit between neutron count rate measured with the radial component of the velocity either positive or negative following the correction as illustrated in Figure 3. This is an approximate correction for the radial component of the Doppler effect.

Following the radial Doppler correction, the tangential component is corrected using an empirical procedure similar to that described in section 2.2.2 to correct for GCR variation. To make this correction, first, the trend in mean epithermal neutron count rate with changing velocity direction is calculated in both the  $x$ -axis and  $y$ -axis directions. This  $y$ -axis-directed trend for the measured data before correction is illustrated in Figure 4, with the trend illustrated with a solid black line. Then as with previous corrections, this empirical trend is removed from the data and model.

#### 2.2.4. Look-Angle Correction

The NS response function varies as a function of spacecraft look direction due to changes in the arrival angle of neutrons into the detector. It is possible to derive an empirical measure of the variation using the data returned during the mission. Look direction is parameterized with the two angles  $\theta$  and  $\phi$ , which are the polar and azimuthal angles of the spacecraft in the spacecraft-fixed coordinate system (i.e.,  $\theta = 0^\circ$  corresponds to the spacecraft  $z$ -axis pointing in the same direction as the spacecraft-to-planet center vector and  $\phi = 0^\circ$  when the spacecraft  $x$ -axis points along the direction of spacecraft motion). To derive this correction, we constructed a two-dimensional histogram, using each measurement, in  $\theta$  and  $\phi$  bins weighted by the detected count rate. As for the nadir- and solid-angle correction in section 2.2.3, to avoid biasing the results due to latitude-dependent compositional variations, we used only the data south of  $45^\circ\text{N}$  to generate the histogram shown in Figure 5. This response map can be understood as showing that for angles where the NS is obstructed by the spacecraft, the response is small (i.e., the mean count rate is low), and for positive angles for which the NS has an unobstructed view of Mercury's surface, the response and thus mean count rate are larger.

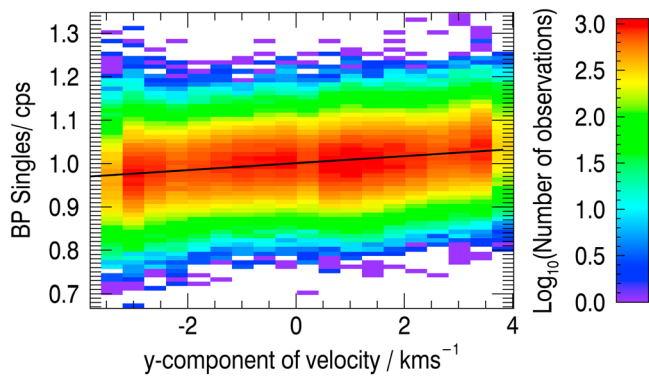


**Figure 4.** Density plot showing the variation in count rate in the measured borated plastic (BP)-singles epithermal data with the component of spacecraft velocity aligned with the spacecraft y-axis. The color shows the density of observations, and the black line is a linear fit to the data points. Detrending the black line from the data forms the tangential Doppler correction. The velocity component is normalized to lie between  $-1$  and  $1$ .

The look-angle correction was performed by using the two-dimensional histogram shown in Figure 5 as a lookup table. For each observation, the average count rate given  $\theta$  and  $\phi$  was found, and the time series count rate was divided through by this average to normalize out the look-angle effects.

### 2.3. MESSENGER GRS Data Reduction

The GRS data reduction follows that described in Peplowski et al. (2011, 2012). As with the neutron data described in the previous section cuts were made to the GRS data to remove data affected by SEP events and EEES. A selection was made to only use data acquired at altitudes less than 2,000 km to ensure a robust SNR. An additional cut was made limiting the data to those with nadir angles less than  $45^\circ$ , again to remove low-SNR regions of the data. The count rate for each line was obtained by fitting a Gaussian peak to the line with a background subtraction as described in Peplowski et al. (2011).

Extensive corrections for spacecraft look direction are not necessary for gamma ray data, as the GRS data will only be used as ratios of lines from a single element and the effects due to look direction on each line should cancel out when the ratio is taken.

a single element and the effects due to look direction on each line should cancel out when the ratio is taken.

#### 2.3.1. Extracting H Abundances From GRS Si Line Ratio

For low hydrogen concentrations (less than  $\sim 0.5$  wt% H), Peplowski, Bazell, et al. (2015) demonstrated a technique for deriving hydrogen concentrations using multiple gamma ray lines with gamma ray data from the Near-Earth Asteroid Rendezvous mission at the asteroid Eros. This technique relies on the detection of two gamma ray lines from a single element originating from inelastic scatter and neutron-capture processes. These two gamma ray emission processes are triggered by neutrons with different energies. Low-energy (thermal) neutrons are more likely to be involved in neutron-capture reactions, and high-energy (fast) neutrons in inelastic scatter reactions. The two important variables in setting the ratio between fast and thermal neutrons are the total macroscopic neutron absorption cross section of the regolith ( $\Sigma_a$ ) and its hydrogen abundance. Thus, if  $\Sigma_a$  is known, the hydrogen abundance can be inferred from measured gamma ray ratios and modeled relationships of the different parameters for realistic variations of elemental abundances. For Mercury's surface  $\Sigma_a$  has been measured using the thermal neutron flux (Peplowski, Bazell, et al., 2015).

In the prior case of the Eros measurements, hydrogen concentrations were measured using the Fe photon ratio between the 846-keV peak resulting from inelastic scatter and the 7,638-keV peak from neutron capture. Due to Mercury's low Fe concentration (Evans et al., 2012), here we use photon ratios for two separate Si lines of 1,778 keV (inelastic scatter) and 4,934 keV (neutron capture). We carried out modeling in MCNPX to find the change in photon ratio with  $\Sigma_a$  and H abundance for a set of three regolith types: the Caloris interior terrane, the intermediate terrane, and the low-Mg northern terrane. The compositions of these terranes are defined in Table 2 of Peplowski, Bazell, et al., 2015. These regolith types span the range of  $\Sigma_a$  seen on Mercury and so form a useful basis for later calculations.

are defined in Table 2 of Peplowski, Bazell, et al., 2015. These regolith types span the range of  $\Sigma_a$  seen on Mercury and so form a useful basis for later calculations.

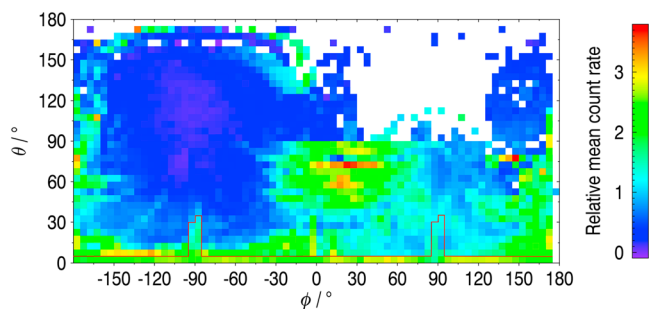


**Figure 5.** The average measured epithermal neutron count rate in  $5^\circ$  look-angle ( $\theta$  and  $\phi$ , defined in the text) bins. These average count rates form the basis of the look-angle correction applied to the data. A similar set are used for the model corrections. Only data below the red line are included following x-axis angle, nadir angle, and other cuts that are made to the data.

## 3. Results

### 3.1. Epithermal Neutron Count Rate Map

The final epithermal neutron maps, obtained after performing all of the corrections described in section 2, are shown in Figure 6. These figures are normalized to show percentage changes around the mean values in both the data and the model. Notably, the map of measured epithermal neutron counts shows a deficit at the north pole. This result agrees with earlier results (Lawrence et al., 2013) that were used to argue for the presence of water ice in the PSRs around Mercury's north pole.

In addition to the polar signature, the count rate map shows variations at the  $3\sigma$  level at the hot poles, implying a statistically significant trend is

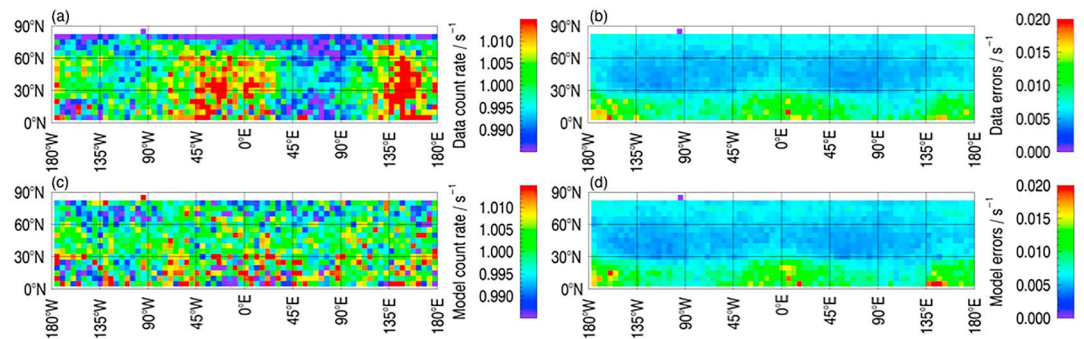


**Figure 6.** The fully corrected (a) measured data and (c) model along with their associated errors in (b) and (d), respectively. The errors are the standard errors on the mean count rate values in each pixel of the epithermal neutron maps using both measured and modeled data.

present in the data. That similar trends are not seen in the model provides confidence that the origin of these variations is due to compositional variations in Mercury’s surface and not due to remaining noncompositional systematic variations.

### 3.2. GRS H Abundances

The absolute hydrogen abundances for the set of regions defined in Table 1 were calculated using the procedure outlined in section 2.3.1 and detailed in Peplowski, David, et al. (2015). The size of the regions was set by requiring that they contain enough data to make a statistically robust measurement of the hydrogen abundances. Additionally, the northern limit of the low-latitude pixels is set by requiring that the hydrogen in the permanently shaded polar craters does not influence the value measured in the pixel. The longitude ranges were chosen to overlap with the count rate highs and lows seen in the neutron data. The measured photon ratios with their associated error ellipses are shown in Figure 7. The mean hydrogen abundance in Mercury’s northern hemisphere is seen to be  $300^{+250}_{-150}$  ppm. Abundances in the other regions are, for the most part, not distinguishable from this within errors, with the exception of the cold poles (CP1 and CP2 in Table 1). CP1 and CP2 hydrogen measurements differ by 2.5- $\sigma$  and 2- $\sigma$ , respectively, from the northern hemispheric mean (‘All’ in Figure 7). That both of these low significance offsets are in the same direction and agree with the neutron map suggests that the increased hydrogen abundance at the cold poles is due to a physical as opposed to statistical origin. The larger-magnitude hydrogen increase suggested at the north pole in the neutron data is not seen in the GRS results due to the large statistical uncertainties in the photon ratio caused by poor counting statistics in this region.

### 3.3. Conversion of Epithermal Neutron Maps to Hydrogen

The absolute hydrogen abundance determined in section 3.2 allows for the conversion of measured epithermal neutron flux into hydrogen abundance. In addition to gamma rays, the particle transport model described in the previous section output neutron fluxes. These neutron fluxes, based on models with different hydrogen abundances, allow for an estimate of how neutron flux changes with hydrogen abundance. The GRS-measured absolute hydrogen abundance allows for this trend to be correctly normalized.

**Table 1**  
*The Locations and Altitude and Nadir Angle Parameters in Each of the Gamma-Ray Spectrometer Regions Examined in Figure 7*

Name	Label	Latitude range (°N)	Longitude range (°E)	Maximum altitude (km)	Maximum nadir angle (°)
North pole	NP	70 to 90	0–360	2,000	45
Hot pole 1	HP1	0 to 55	120–180	2,400	45
Hot pole 2	HP2	0 to 55	280–360	2,400	45
Cold pole 1	CP1	0 to 55	30–110	2,400	45
Cold pole 2	CP2	0 to 55	210–290	2,400	45
Equatorial	EQ	20 to 70	0–360	2,000	60
All	All	–20 to 90	0–360	2,000	60

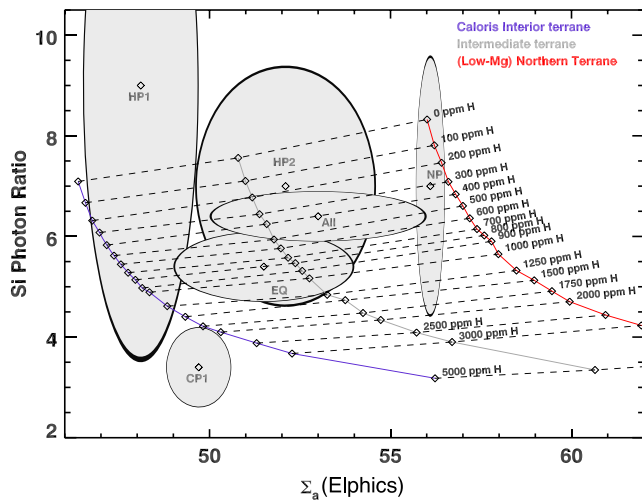


**Figure 7.** The silicon photon ratio and total macroscopic neutron absorption cross section,  $\Sigma_a$ , for the regions defined in Table 1. The cross section is shown in units of Elphics defined as  $10^{-4} \text{ cm}^2/\text{g}$ . The grid shows the result of MCNPX simulations with three different regolith types and the various hydrogen abundances indicated in the figure. The ellipses show the  $1-\sigma$  errors on the measurements.

The epithermal neutron map, showing a conversion to hydrogen abundances, is presented in Figure 8. This map has also been smoothed with a Gaussian kernel whose width matches the resolution of the instrument, which changes with latitude. This smoothing was done to reduce the visibility of the noise that can be seen in Figure 6a. At the resolution of the MESSENGER neutron measurements, the footprint-averaged increase in hydrogen seen at the north pole is  $\sim 75$  ppm, which is consistent with earlier work showing a 50- to 100-ppm H increase at high latitudes (Lawrence et al., 2013). Using both epithermal and fast neutron data, this earlier result was shown to be consistent with the radar-bright regions containing a hydrogen-rich layer buried beneath a desiccated layer 10–30 cm deep. In the midlatitudes, the hydrogen abundance appears to vary periodically with wavelength of  $180^\circ$  in the longitudinal direction. It is interesting to note that maximum and mean surface and near-subsurface temperatures on Mercury also vary with latitude due to its 3:2 spin-orbit resonance. This resonance leads to the presence of hot poles (at  $0^\circ\text{E}$  and  $180^\circ\text{E}$ ) that always experience noon at perihelion and cold poles (at  $90^\circ\text{E}$  and  $270^\circ\text{E}$ ) that experience noon at aphelion (Vasavada et al., 1999). The hydrogen lows of  $\sim 365$  ppm are approximately coincident with the hot poles, and the highs ( $\sim 400$  ppm) are approximately collocated with the cold poles. A hydrogen correlation with mean or maximum temperature might be explained as a thermal stability/mobility effect, the result of

implantation differences, or as the effect of mineralogy. These and other correlations are examined further in the next section.

#### 4. Comparison of Hydrogen Abundance and Other Data

In this section we will examine the correlation between the hydrogen abundance as revealed by the GRS and epithermal neutron data and other data sets. As observed in the previous section there appears to be a relationship between hydrogen abundance and surface/near-surface temperature. This might be explained by a temperature-dependent stability effect in controlling where hydrogen is present in Mercury's near subsurface. However, additional trends might also be expected. For example, on the Moon a correlation is seen between epithermal measured hydrogen abundance and other measures of maturity including crater density and optical maturity, which is explained as the result of solar wind proton implantation over time (Lawrence, Patrick, et al., 2015). In addition, one might expect correlations between hydrogen and other

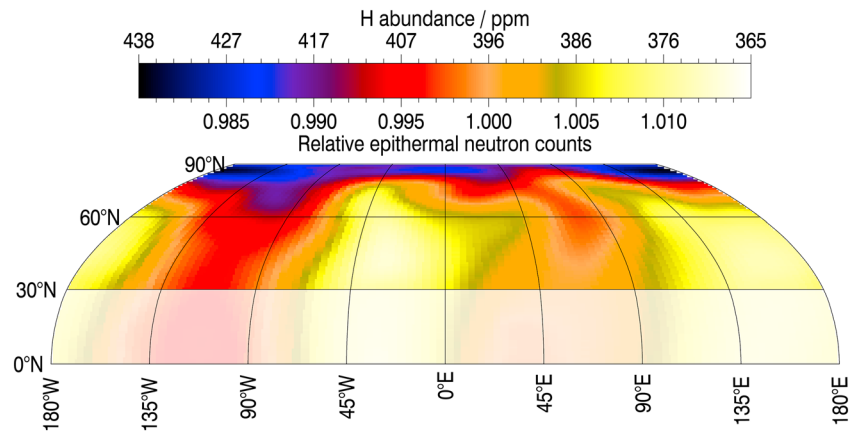


**Figure 8.** Northern hemisphere Robinson projection showing the smoothed epithermal flux with a conversion to hydrogen abundance in parts per million based on Gamma-Ray Spectrometer results and particle transport modeling. The grayed out region south of  $30^\circ\text{N}$  highlights the low signal-to-noise ratio data.



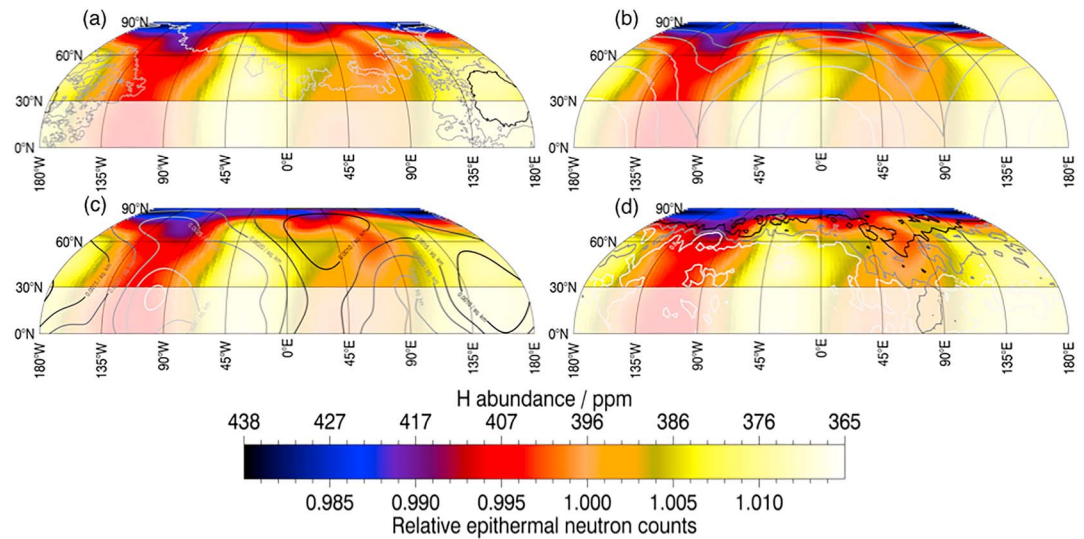


**Figure 9.** The corrected epithermal neutron flux overlain by contours showing: (a) The smooth plains terrains (Denevi et al., 2013); Caloris basin plains outline in black; Caloris ejecta plains surrounding the basin in gray; and the northern smooth plains in gray at the pole. (b) Maximum surface temperature in K from Paige et al. (2013). (c) Crater density derived using kernel density estimation based on the catalogue in Fassett et al. (2011; Figure 11). (d) Mercury Maturity Index as originally described in Neish et al. (2013; Figure 12).

elements if the regolith type affects hydrogen implantation or stability. We will look for these effects using the various data sets described below.

#### 4.1. Smooth Plains Unit

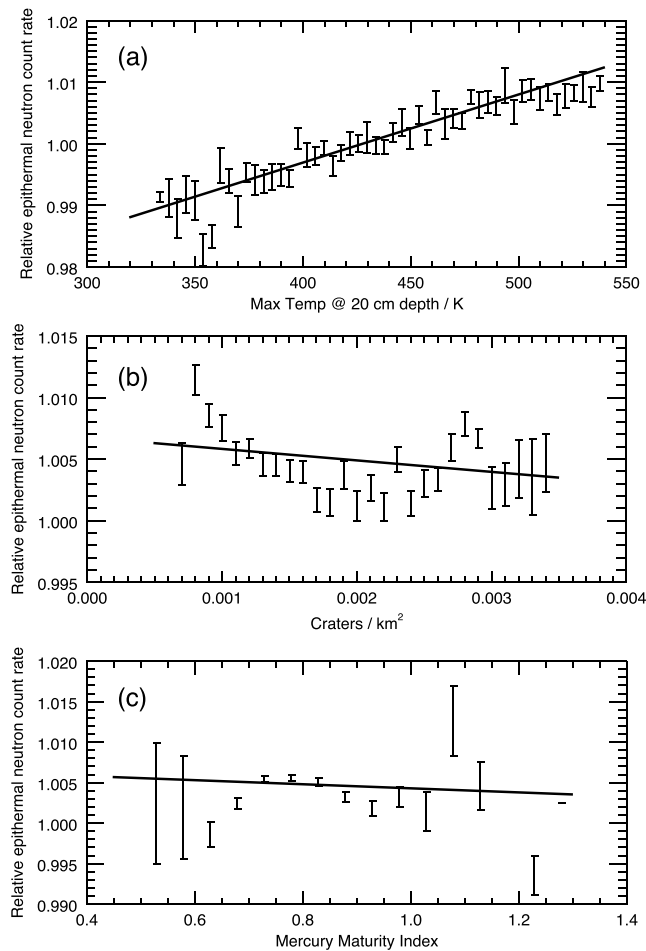
Approximately 27% of Mercury's surface is covered by smooth plains units, which have relatively low crater densities implying ages younger than the end of the late heavy bombardment (e.g., Trask & Guest, 1975; Denevi et al., 2013). The majority of these plains are believed to result from volcanic flows, though some regions may be the result of deposition of fluidized ejecta (Denevi et al., 2013). These plains are analogous to the lunar maria, also emplaced after the cessation of the late heavy bombardment. However, unlike the lunar maria, they do not show large albedo differences from the surrounding areas, which would be suggestive of compositional differences. Either as a result of the difference in age or as a result of possible differences in composition, we might expect the smooth plains units to contain a hydrogen signature distinct from their surroundings.

Figure 9a shows the outline of the smooth plains identified in Denevi et al. (2013) as contours on the epithermal/hydrogen map. No correlation is seen between these two data sets other than the increase in H at the north pole being approximately coincident with the northern smooth plain. However, this is most likely a coincidence caused by the presence of ice-bearing permanently shaded craters at the pole as the longitudinal asymmetry in the northern smooth plains is not seen in the neutron data. Caloris does overlap with a region depleted in hydrogen. However, the hydrogen depletion 180° from Caloris does not have a smooth plains counterpart.

#### 4.2. Temperature

In our comparison between temperatures and hydrogen, we considered both mean and maximum temperatures at a range of depths between the top surface and 20 cm using the results of the thermal model described in Peplowski et al. (2012) using the formalism of Vasavada et al. (1999). The correlation between temperature and epithermal neutron flux was found to be strongest for the maximum temperature at 20-cm depth, the mean depths from which neutrons originate (with Pearson correlation coefficient of  $0.6 \pm 0.02$  compared with  $0.5 \pm 0.02$  for correlation with surface temperature), and this is shown as a contour in Figure 9b.

The correlation between near-surface temperature and epithermal neutron counts in the midlatitudes is shown clearly in Figure 10a. A strong positive trend is seen in the data, which corresponds to decreasing hydrogen abundance with increasing temperature. It is interesting to note that the hotter areas on the



**Figure 10.** Plots of (a) maximum surface temperature, (b) crater density, and (c) Mercury Maturity Index against corrected measured epithermal neutron count rate normalized to a mean of 1. The plots are restricted to latitudes between 30°N and 60°N to avoid the effects of the polar hydrogen deposits and low-signal-to-noise ratio region close to the equator.

surface also receive a greater daily average solar wind flux due to Mercury's spin-orbit resonance, which we might expect to lead to higher hydrogen abundance. That this trend is not seen suggests that the thermal stability effects outweigh the effect of solar wind implantation despite the fact that the cumulative precipitation of solar wind ions varies by 2 orders of magnitude across the surface (Pfleger et al., 2015).

### 4.3. Crater Density

Crater density is a proxy for surface age and on the Moon is seen to be correlated with epithermal-derived hydrogen abundance (Lawrence et al., 2013). We look for a similar relationship on Mercury using the database of craters greater than 20 km compiled by Fassett et al. (2011). This database was converted into a map of crater density using the method of kernel density estimation (Parzen, 1962; Rosenblatt, 1956) with Gaussian kernels, chosen for smoothness. The bandwidth was chosen using a four-fold cross-validation technique (Rudemo, 1982), and the optimal width was found to be 480 km. The resulting crater density map is shown in Figure 11 and plot as a contour in Figure 9c.

The crater density is low around Caloris, corresponding to a region depleted in hydrogen, and greatest around 90°W and 30°N where the hydrogen abundance is low for that latitude. The strength of the midlatitude correlation is shown in Figure 10b. The trend is in the expected direction (i.e., older, more cratered surfaces have more hydrogen); however, the correlation is not strong. Given the broad size of the kernel used in generating the map, the correlation may simply be the result of the coincident overlap of Caloris with a hot pole and the crater density high with a cold pole.

### 4.4. Mercury Maturity Index

As the Moon's surface is weathered by micrometeoroid bombardment and the action of solar wind ions, it both darkens and reddens (i.e., the reflectance decreases more sharply at shorter than longer wavelengths). The main cause of these effects is the accumulation of nanophase iron due to the reduction of ferrous iron silicates. Lucey et al. (2000) defined the OMAT parameter to distinguish this optical maturity from composition-

dependent spectral slopes and albedo changes. It is defined as the Euclidean distance, in a 750-nm reflectance versus 950- to 750-nm reflectance ratio space, between a reference point and the measured value. Where the reference point is defined empirically for each instrument. Due to the high utility of OMAT in

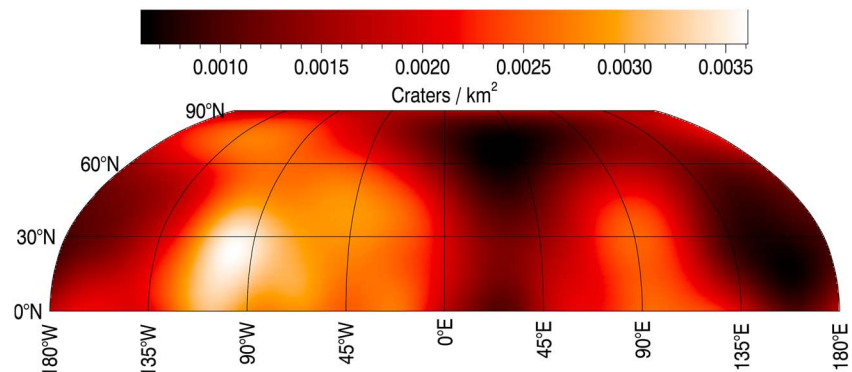


**Figure 11.** The crater density on Mercury derived from the database of craters of greater than 20 km diameter in Fassett et al. (2011).

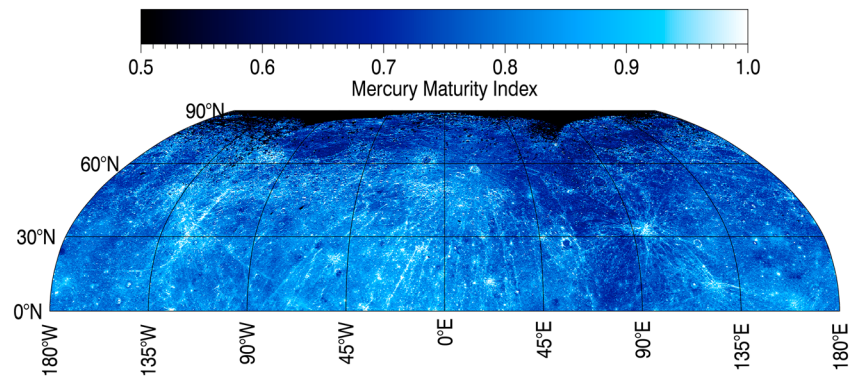


**Figure 12.** The MDIS-derived Mercury Maturity Index, higher values indicate younger material.

lunar studies, a similar optical maturity measure was created for Mercury called MMI (Neish et al., 2013); as with OMAT, MMI is inversely proportional to maturity. MMI is defined as the mean reflectance in MESSENGER MDIS normalized by the spectral slope across the instrument's eight channels. For this study we used the up-to-date eight-color Map-Projected Multispectral Reduced Data Record (MDR) mosaics (<http://messenger.jhuapl.edu/Explore/Images.html#global-mosaics>). These data are the result of combining the MDIS MDR wide-angle camera multispectral data records available on the PDS at [https://pdsimage2.wr.usgs.gov/data/mess-h-mdis-5-rdr-mdr-v1.0/MSGRMDS\\_5001/MDR/](https://pdsimage2.wr.usgs.gov/data/mess-h-mdis-5-rdr-mdr-v1.0/MSGRMDS_5001/MDR/). The resulting MMI map is shown in Figure 12, and the data are provided as supporting information.

The most noticeable small-scale features in the MMI map are the young, bright-rayed craters. Larger trends are also seen; there is a broad decrease in MMI between 75°E and 90°E. These are more evident in the contours in Figure 9d, which shows the overlap between this older, low-MMI region and the midlatitude hydrogen abundance. The strength of the MMI-H correlation is shown in Figure 10c and is seen to be weak to null. That there is little correlation between MMI and H again suggests that implantation plays little role in determining the present-day hydrogen distribution on Mercury's surface.

#### 4.5. XRS Chemical Abundance Maps

To look for mineralogical explanations of the hydrogen distribution, we also compared the epithermal-measured hydrogen distribution with the publicly available X-ray Spectrometer (XRS) element ratio maps including Fe, Mg/Si, and Al/Si (Weider et al., 2015). However, no correlation was seen between epithermal neutron flux and any of the XRS data.

## 5. Conclusions

Using the MESSENGER GRS Si line ratio and NS BP sensor epithermal neutron data we found the mean absolute hydrogen abundance in Mercury's northern hemisphere to be  $300^{+250}_{-150}$  ppm and produced a map of its distribution. We found an increase in hydrogen concentration, averaged over the instrument's footprint, of 75 ppm, moving from the midlatitudes to the north pole. This increase is in agreement with the earlier analysis of Lawrence et al. (2013) who showed that the neutron data are consistent with the polar hydrogen excess being contained in a hydrogen-rich layer within the radar-bright regions identified as water-bearing permanently shaded craters. An additional longitudinal trend in epithermal neutron count rate or hydrogen abundance was seen that correlates well with maximum temperature at 20-cm depth and less strongly with crater density (a measure of surface age) between 30°N and 60°N. These results imply the presence of hydrogen in Mercury's midlatitudes is strongly temperature dependent.

## References

- Black, G. J., Campbell, D. B., & Harmon, J. K. (2010). Radar measurements of Mercury's north pole at 70 cm wavelength. *Icarus*, 209(1), 224–229. <https://doi.org/10.1016/j.icarus.2009.10.009>
- Boynton, W. V., Feldman, W. C., Squires, S. W., Prettyman, T. H., Brückner, J., Evans, L. G., et al. (2002). Distribution of Hydrogen in the Near Surface of Mars: Evidence for Subsurface Ice Deposits. *Science*, 297(5578), 81–85. <https://doi.org/10.1126/science.1073722>

### Acknowledgments

The authors thank Dave Blewett for his help in preparing the Mercury maturity index data. The raw neutron data are available on NASA's PDS at [http://pds-geosciences.wustl.edu/missions/messenger/ns\\_edr.html](http://pds-geosciences.wustl.edu/missions/messenger/ns_edr.html) and the gamma ray data at [http://pds-geosciences.wustl.edu/missions/messenger/grs\\_edr.html](http://pds-geosciences.wustl.edu/missions/messenger/grs_edr.html). The reduced neutron map and errors are available as supporting information. J. T. W., D. J. L., and P. N. P. acknowledge support from the MESSENGER Participating Scientist Program.

- Butler, B. J., Muhleman, D. O., & Slade, M. A. (1993). Mercury—Full-disk radar images and the detection and stability of ice at the north pole. *Journal of Geophysical Research*, *98*, 15,003–15,023. <https://doi.org/10.1029/93JE01581>
- Chabot, N. L., Ernst, C. M., Denevi, B. W., Nair, H., Deutsch, A. N., Blewett, D. T., et al. (2014). Images of surface volatiles in Mercury's polar craters acquired by the MESSENGER spacecraft. *Geology*, *42*(12), 1051–1054. <https://doi.org/10.1130/G35916.1>
- Denevi, B. W., Ernst, C. M., Meyer, H. M., Robinson, M. S., Murchie, S. L., Whitten, J. L., et al. (2013). The distribution and origin of smooth plains on Mercury. *Journal of Geophysical Research: Planets*, *118*, 891–907. <https://doi.org/10.1002/jgre.20075>
- Evans, L. G., Peplowski, P. N., Rhodes, E. A., Lawrence, D. J., McCoy, T. J., Nittler, L. R., et al. (2012). Major-element abundances on the surface of mercury: Results from the MESSENGER Gamma-Ray Spectrometer. *Journal of Geophysical Research*, *117*, E00L07. <https://doi.org/10.1029/2012JE004178>
- Evans, L. G., & Squyres, S. W. (1987). Investigation of Martian H<sub>2</sub>O and CO<sub>2</sub> via orbital gamma ray spectroscopy. *Journal of Geophysical Research*, *92*, 9153–9167. <https://doi.org/10.1029/JB092iB09p09153>
- Fassett, C. I., Kadish, S. J., Head, J. W., Solomon, S. C., & Strom, R. G. (2011). The global population of large craters on Mercury and comparison with the Moon. *Geophysical Research Letters*, *38*, L10202. <https://doi.org/10.1029/2011GL047294>
- Feldman, W. C., & Drake, D. M. (1986). A Doppler filter technique to measure the hydrogen content of planetary surfaces. *Nuclear Instruments and Methods in Physics Research Section A: Accelerators, Spectrometers, Detectors and Associated Equipment*, *245*(1), 182–190. [https://doi.org/10.1016/0168-9002\(86\)90274-3](https://doi.org/10.1016/0168-9002(86)90274-3)
- Feldman, W. C., Drake, D. M., O'Dell, R. D., Brinkley, F. W. Jr., & Anderson, R. C. (1989). Gravitational effects on planetary neutron flux spectra. *Journal of Geophysical Research*, *94*, 513–525. <https://doi.org/10.1029/JB094iB01p00513>
- Goldsten, J. O., Rhodes, E. A., Boynton, W. V., Feldman, W. C., Lawrence, D. J., Trombka, J. I., et al. (2007). The MESSENGER Gamma-Ray and Neutron Spectrometer. *Space Science Reviews*, *131*(1–4), 339–391. <https://doi.org/10.1007/s11214-007-9262-7>
- Harcke, L. J. (2005). Radar imaging of solar system ices. (PhD thesis). Stanford University, CA.
- Harmon, J. K., Perillat, P. J., & Slade, M. A. (2001). High-resolution radar imaging of Mercury's north pole. *Icarus*, *149*(1), 1–15. <https://doi.org/10.1006/icar.2000.6544>
- Harmon, J. K., & Slade, M. A. (1992). Radar mapping of mercury—Full-disk images and polar anomalies. *Science*, *258*(5082), 640–643. <https://doi.org/10.1126/science.258.5082.640>
- Harmon, J. K., Slade, M. A., Vélez, R. A., Crespo, A., Dryer, M. J., & Johnson, J. M. (1994). Radar mapping of Mercury's polar anomalies. *Nature*, *369*(6477), 213–215. <https://doi.org/10.1038/369213a0>
- Lawrence, D. J., Anderson, B. J., Baker, D. N., Feldman, W. C., Ho, G. C., Korth, H., et al. (2015). Comprehensive survey of energetic electron events in Mercury's magnetosphere with data from the MESSENGER Gamma-Ray and Neutron Spectrometer. *Journal of Geophysical Research: Space Physics*, *120*, 2851–2876. <https://doi.org/10.1002/2014JA020792>
- Lawrence, D. J., Feldman, W. C., Goldsten, J. O., Maurice, S., Peplowski, P. N., Anderson, B. J., et al. (2013). Evidence for water ice near Mercury's north pole from MESSENGER Neutron Spectrometer measurements. *Science*, *339*(6117), 292–296. <https://doi.org/10.1126/science.1229953>
- Lawrence, D. J., Harmon, J. K., Feldman, W. C., Goldsten, J. O., Paige, D. A., Peplowski, P. N., et al. (2011). Predictions of MESSENGER Neutron Spectrometer measurements for Mercury's north polar region. *Planetary and Space Science*, *59*(13), 1665–1669. <https://doi.org/10.1016/j.pss.2011.07.001>
- Lawrence, D. J., Peplowski, P. N., Feldman, W. C., Schwadron, N. A., & Spence, H. E. (2016). Galactic cosmic ray variations in the inner heliosphere from solar distances less than 0.5 AU: Measurements from the MESSENGER Neutron Spectrometer. *Journal of Geophysical Research: Space Physics*, *121*, 7398–7406. <https://doi.org/10.1002/2016JA022962>
- Lawrence, D. J., Feldman, W. C., Goldsten, J. O., McCoy, T. J., Blewett, D. T., Boynton, W. V., et al. (2010). Identification and measurement of neutron-absorbing elements on Mercury's surface. *Icarus*, *209*(1), 195–209. <https://doi.org/10.1016/j.icarus.2010.04.005>
- Lawrence, D. J., Peplowski, P. N., Beck, A. W., Feldman, W. C., Frank, E. A., McCoy, T. J., et al. (2017). Compositional terranes on Mercury: Information from fast neutrons. *Icarus*, *281*, 32–45. <https://doi.org/10.1016/j.icarus.2016.07.018>
- Lawrence, D. J., Peplowski, P. N., Plescia, J. B., Greenhagen, B. T., Maurice, S., & Prettyman, T. H. (2015). Bulk hydrogen abundances in the lunar highlands: Measurements from orbital neutron data. *Icarus*, *255*, 127–134. <https://doi.org/10.1016/j.icarus.2015.01.005>
- Lucey, P. G., Blewett, D. T., Taylor, G. J., & Hawke, B. R. (2000). Imaging of lunar surface maturity. *Journal of Geophysical Research*, *105*, 20,377–20,386. <https://doi.org/10.1029/1999JE001110>
- Maurice, S., Lawrence, D. J., Feldman, W. C., Elphic, R. C., & Gasnault, O. (2004). Reduction of neutron data from Lunar Prospector. *Journal of Geophysical Research*, *109*, E07S04. <https://doi.org/10.1029/2003JE002208>
- Maurice, S., Feldman, W., Diez, B., Gasnault, O., Lawrence, D., Pathare, A., & Prettyman, T. (2011). Mars Odyssey neutron data: 1. Data processing and models of water-equivalent-hydrogen distribution. *Journal of Geophysical Research*, *116*, E11008. <https://doi.org/10.1029/2011JE003810>
- Neish, C. D., Blewett, D. T., Harmon, J. K., Coman, E. I., Cahill, J. T. S., & Ernst, C. M. (2013). A comparison of rayed craters on the Moon and Mercury. *Journal of Geophysical Research: Planets*, *118*, 2247–2261. <https://doi.org/10.1002/jgre.20166>
- Neumann, G. A., Cavanaugh, J. F., Sun, X., Mazarico, E. M., Smith, D. E., Zuber, M. T., Mao, D., et al. (2013). Bright and dark polar deposits on Mercury: Evidence for surface volatiles. *Science*, *339*(6117), 296–300. <https://doi.org/10.1126/science.1229764>
- Nikoukar, R., Lawrence, D. J., Peplowski, P. N., Dewey, R. M., Korth, H., Baker, D. N., & McNutt, R. L. Jr. (2018). Statistical study of Mercury's energetic electron events as observed by the Gamma-Ray and Neutron Spectrometer instrument onboard MESSENGER. *Journal of Geophysical Research: Space Physics*, *123*, 4961–4978. <https://doi.org/10.1029/2018JA025339>
- Paige, D. A., Siegler, M. A., Harmon, J. K., Neumann, G. A., Mazarico, E. M., Smith, D. E., et al. (2013). Thermal stability of volatiles in the north polar region of Mercury. *Science*, *339*(6117), 300–303. <https://doi.org/10.1126/science.1231106>
- Paige, D. A., Wood, S. E., & Vasavada, A. R. (1992). The thermal stability of water ice at the poles of Mercury. *Science*, *258*(5082), 643–646. <https://doi.org/10.1126/science.258.5082.643>
- Parzen, E. (1962). Estimation of a probability density-function and mode. *Annals of Mathematical Statistics*, *33*(3), 1065–1076. <https://doi.org/10.1214/aoms/1177704472>
- Peplowski, P. N., Bazell, D., Evans, L. G., Goldsten, J. O., Lawrence, D. J., & Nittler, L. R. (2015). Hydrogen and major element concentrations on 433 Eros: Evidence for an L- or LL-chondrite-like surface composition. *Meteoritics and Planetary Science*, *50*(3), 353–367. <https://doi.org/10.1111/maps.12434>
- Peplowski, P. N., Lawrence, D. J., Rhodes, E. A., Sprague, A. L., McCoy, T. J., Denevi, B. W., et al. (2012). Variations on the abundances of potassium and thorium on the surface of mercury: Results from the MESSENGER Gamma-Ray Spectrometer. *Journal of Geophysical Research*, *117*, E00L04. <https://doi.org/10.1029/2012JE004141>

- Peplowski, P. N., Lawrence, D. J., Feldman, W. C., Goldsten, J. O., Bazell, D., Evans, L. G., et al. (2015). Geochemical terranes of Mercury's northern hemisphere as revealed by MESSENGER neutron measurements. *Icarus*, *253*, 346–363. <https://doi.org/10.1016/j.icarus.2015.02.002>
- Peplowski, P. N., Nittler, L. R., Hauck, S. A., McCoy, T. J., Boynton, W. V., Gillis-Davis, J. J., et al. (2011). Radioactive elements on Mercury's surface from MESSENGER: Implications for the Planet's formation and evolution. *Science*, *333*(6051), 1850–1852. <https://doi.org/10.1126/science.1211576>
- Pfleger, M., Lichtenegger, H. I. M., Wurz, P., Lammer, H., Kallio, E., Alho, M., et al. (2015). 3D-modeling of Mercury's solar wind sputtered surface-exosphere environment. *Planetary and Space Science*, *115*, 90–101. <https://doi.org/10.1016/j.pss.2015.04.016>
- Rosenblatt, M. (1956). Remarks on some nonparametric estimates of a density-function. *Annals of Mathematical Statistics*, *27*(3), 832–837. <https://doi.org/10.1214/aoms/117728190>
- Rudemo, M. (1982). Empirical choice of histograms and kernel density estimators. *Scandinavian Journal of Statistics*, *9*(2), 65–78.
- Slade, M. A., Butler, B. J., & Muhleman, D. O. (1992). Mercury radar imaging—Evidence for polar ice. *Science*, *258*(5082), 635–640. <https://doi.org/10.1126/science.258.5082.635>
- Solomon, S. C., McNutt, R. L., Gold, R. E., & Domingue, D. L. (2007). MESSENGER Mission overview. *Space Science Reviews*, *131*(1-4), 3–39. <https://doi.org/10.1007/s11214-007-9247-6>
- Stark, A., Oberst, J., Preusker, F., Gwinner, K., Peale, S. J., Margot, J.-L., et al. (2015). First MESSENGER orbital observations of Mercury's librations. *Planetary and Space Science*, *117*, 64–72. <https://doi.org/10.1016/j.pss.2015.05.006>
- Trask, N. J., & Guest, J. E. (1975). Preliminary geologic terrain map of Mercury. *Journal of Geophysical Research*, *80*, 2461–2477. <https://doi.org/10.1029/JB080i017p02461>
- Vasavada, A. R., Paige, D. A., & Wood, S. E. (1999). Near-surface temperatures on Mercury and the Moon and the stability of polar ice deposits. *Icarus*, *141*(2), 179–193. <https://doi.org/10.1006/icar.1999.6175>
- Weider, S. Z., Nittler, L. R., Starr, R. D., Crapster-Pregont, E. J., Peplowski, P. N., Denevi, B. W., et al. (2015). Evidence for geochemical terranes on Mercury: Global mapping of major elements with MESSENGER's X-Ray Spectrometer. *Earth and Planetary Science Letters*, *416*, 109–120. <https://doi.org/10.1016/j.epsl.2015.01.023>